SIAM J. APPL. MATH.
Vol. 66, No. 5, pp. 1512–1532
© 2006 Society for Industrial and Applied Mathematics

PERMEABILITY HYSTERESIS IN GRAVITY COUNTERFLOW SEGREGATION*

C. E. SCHAERER†, M. SARKIS‡, D. MARCHESIN†, AND P. BEDRIKOVETSKY§

Abstract. Hysteresis effects in two-phase flow in porous media are important in applications such as waterflooding or gas storage in sand aquifers. In this paper, we develop a numerical scheme for such a flow where the permeability hysteresis is modeled by a family of reversible scanning curves enclosed by irreversible imbibition and drainage permeability curves. The scheme is based on associated local Riemann solutions and can be viewed as a modification of the classical Godunov method. The Riemann solutions necessary for the scheme are presented, as well as the criteria that guarantee the well-posedness of the Riemann problem with respect to perturbations of left and right states. The numerical and analytical results show strong influence of the permeability hysteresis on the flow. In addition, the numerical scheme accurately reproduces the available experimental data once hysteresis is taken into account in the model.

Key words. relative permeability, hysteresis, Riemann problem, conservation laws, two-phase flow in porous media, Godunov method

AMS subject classifications. 74N30, 76T10, 35L65, 74S10

DOI. 10.1137/040616061

1. Introduction.

Capillary hysteresis strongly affects two-phase flow in porous media during sequential increase and decrease of wetting phase saturation (i.e., during the so-called imbibition and drainage, respectively) [6, 8]. The alternation of imbibition and drainage occurs in several oil recovery processes. It occurs in waterflooding with displacement direction change due to redistribution of injection and production rates in a system of wells, WAG (water-alternate-gas) injection of sequences of water and gas slugs, and sequential injection and production in the same well [4]. Annual injection and production of natural gas in aquifers or in depleted petroleum reservoirs for storage purposes also result in significant hysteretic phenomena. A similar flow regime change phenomenon, from imbibition to drainage and vice versa, occurs in secondary migration of hydrocarbons during the formation of petroleum accumulations [1], in irrigation, and in soil contamination by gasoline.

Capillary hysteresis at a macroscopic scale is caused by several pore scale phenomena. The contact angle on menisci between wetting and nonwetting phases suffers hysteresis during flow changes in a single pore. Creation of new interfacial surfaces resulting in energy losses occurs during imbibition; on the contrary, energy is released during drainage due to oil droplet joining. All these phenomena result in different scenarios of porous space filling by wetting and nonwetting phases.

*Received by the editors September 30, 2004; accepted for publication (in revised form) January 26, 2006; published electronically May 26, 2006.
http://www.siam.org/journals/siap/66-5/61606.html

†Instituto de Matemática Pura e Aplicada–IMPA, E. D. Castorina 110, 22460-320, Rio de Janeiro, RJ, Brazil (cschaer@fluid.impa.br, marchesi@impa.br). The research of the first and third authors was partially supported by FAPERJ (E-26/152.254/2002, E-26/152.163/2002) and by CNPq (500075/2002-6, 301532/2003-6).

‡Worcester Polytechnic Institute, Worcester, MA 01609 (msarkis@impa.br). The research of this author was partially supported by CNPq (Brazil) under grant 305539/2003-8 and by the U.S. National Science Foundation under grant CGR 9984404.

§Petroleum Department, North Fluminense State University, R. Sebastião Lopes da Silva 56, Macaé, 27937-150 RJ, Brazil (pavel@lenep.uenf.br).

Models for multiphase flow in porous media are based on conservation of mass and Darcy's law. The associated equations contain quantities describing the rock and fluid properties, in particular relative phase permeabilities. The latter describe the capability of each phase to flow in the porous medium [2, 9]. Relative permeability of the nonwetting phase exhibits hysteresis or memory effects [10], i.e., according to the saturation tendency, the relative permeability is different [18].

The model for hysteretic relative permeability of the nonwetting phase [2, 12] follows experimental observations of drainage, imbibition, and scanning behavior of relative permeability [6, 7, 8, 13, 19]. Changes in the direction of the flow in drainage and imbibition are irreversible [6, 18]; flow in the region between drainage and imbibition curves is in general almost reversible [8, 19, 17]; however, we will make the approximation that it is exactly reversible [6, 13].

Observations and explanations of permeability hysteresis in laboratory experiments for horizontal one-dimensional flow were presented in several works [17, 6, 8]. However, mathematical understanding is insufficient, hindering the inclusion of hysteresis in numerical simulation of reservoir flow. Formulae for drainage, imbibition, and scanning relative permeabilities curves were developed in [2, 12], among others. In [15], only the imbibition and drainage curves were considered. A model that we will call the scanning hysteresis model (SHM) for the history dependence of the relative permeabilities was presented in [10] and in [18].

In the current work, we concentrate on hysteretic gravity segregation. This phenomenon occurs after waterflooding or after gas injection in thick oil formations. It also occurs in in-situ gas storage in thick formations between injection and production cycles. Estimation of the gravity separation time is necessary for planning of tertiary recovery from reformed formations.

Our goal is to develop a numerical tool for the gravitational counterflow segregation problem with a hysteretic relative permeability. Because Riemann solutions with hysteresis in the relative permeability are not unique, we introduce criteria to obtain well-posedness with respect to left and right states. In the large scale approximation formulation, we do not include the capillarity pressure and its hysteresis [4].

The paper is organized as follows: In section 2, we present the model for two-phase gravity counterflow segregation. In addition, we extend the SHM for the nonwetting relative permeability [18] to include gravity. This model associates a hysteretic parameter π in order to "remember" the value of the saturation at the last time when the saturation tendency was reversed. In the equations used to model the segregation, the capillary forces and its hysteresis affect both the transport part and the diffusive part. We concentrate on the hysteresis in relative permeability. In section 3, the Riemann solutions for the hysteretic conservation law are discussed. Criteria to select a unique well-posed solution are developed. In section 4, we propose a corrected Godunov scheme that updates both the saturation and the hysteretic states. This scheme conserves mass locally. Finally, in section 5, we show that the numerical solution of the Riemann problem converges to the exact solution. Comparisons of the numerical solution (with and without hysteresis) with laboratory data are presented. They show that hysteresis must be taken into account to obtain correct predictions of segregation. Additionally, it is demonstrated that the proposed numerical method captures adequately the experimental profiles, and the main hysteresis effects can be modeled through the relative permeability curves.

2. The two-phase model for gravity counterflow segregation. We consider a sand-packed vertical tube with a given initial saturation profile of two incom-

pressible immiscible fluids. Redistribution of the fluids with different densities occurs due to gravitational forces. The total flow along the tube is zero as the tube is closed at the top and bottom. Neglecting diffusive terms due to capillarity relative to gravitational forces, the two-phase flow model equation expressing mass conservation and Darcy's law in dimensionless variables (z,t), $\{0 \le z \le 1, t \ge 0\}$ is [4]

$$\partial_t s + \partial_z F(s,\pi) = 0, \tag{2.1}$$

where the flow function $F(s,\pi)$ is

$$F(s,\pi) := \frac{k_{rw}k_{ro}}{k_{ro} + (\mu_o/\mu_w)k_{rw}}. \tag{2.2}$$

We use the indices w and o to refer to the wetting and nonwetting phases, respectively. The quantities k_{rw} (k_{ro}) and μ_w (μ_o) are the relative permeability and the viscosity of the wetting phase w (nonwetting o), respectively. In the absence of hysteresis, k_{rw} (k_{ro}) are functions of the effective wetting phase saturation s defined as

$$s := \frac{s_w - s_{wi}}{s_{ro} - s_{wi}}, \tag{2.3}$$

where s_{wi} is the irreducible wetting saturation and s_{ro} is the residual nonwetting saturation.

2.1. The SHM: Mathematical description. To model the hysteresis phenomenon observed experimentally in the relative permeabilities [6], we extend the SHM presented in [10, 18] to include gravity. For simplicity, the nonwetting phase exhibits hysteresis, while the wetting phase does not. In order to describe the behavior due to hysteresis, a parameter π is introduced. Concretely, we generalize the permeability functions presented in [18] and use the following special permeability functions of the effective saturation s [3].

The wetting relative permeability is defined as (Figure 2.1(a))

$$k_{rw}(s) := \gamma s^{\beta},\ \beta > 1, \tag{2.4}$$

where γ is a parameter to adjust the curve (2.4) to the relative permeability curve obtained experimentally, so that $k_{rw}(1) = \gamma$, as the nonwetting permeability is normalized as 1 for $s = 0$.

The nonwetting drainage and imbibition relative permeabilities functions (expressed by k^d_{ro} and k^i_{ro}) are defined as (Figure 2.1(a)) [3]

$$\begin{aligned} k^d_{ro}(s) &= (1-s)^{\eta} \quad \text{for } 0 \le s \le 1 \quad \text{and when } \frac{\partial s}{\partial t} < 0, \\ k^i_{ro}(s) &= (1-s)^{\theta} \quad \text{for } 0 \le s \le 1 \quad \text{and when } \frac{\partial s}{\partial t} > 0, \end{aligned} \tag{2.5}$$

where $1 < \theta < \eta$. In this paper, we use $\beta = 2$, $\eta = 3$, and $\theta = 2$; therefore $k^d_{ro} \le k^i_{ro}$.

The scanning region corresponds to the region between the nonwetting drainage and imbibition relative permeabilities curves. In such a region the nonwetting permeability k_{ro} is chosen as

$$k_{ro}(s,\pi) := \frac{(1-\pi)^{\xi}}{(1-\alpha\pi)^{\zeta}}(1-\alpha s)^{\zeta}, \tag{2.6}$$

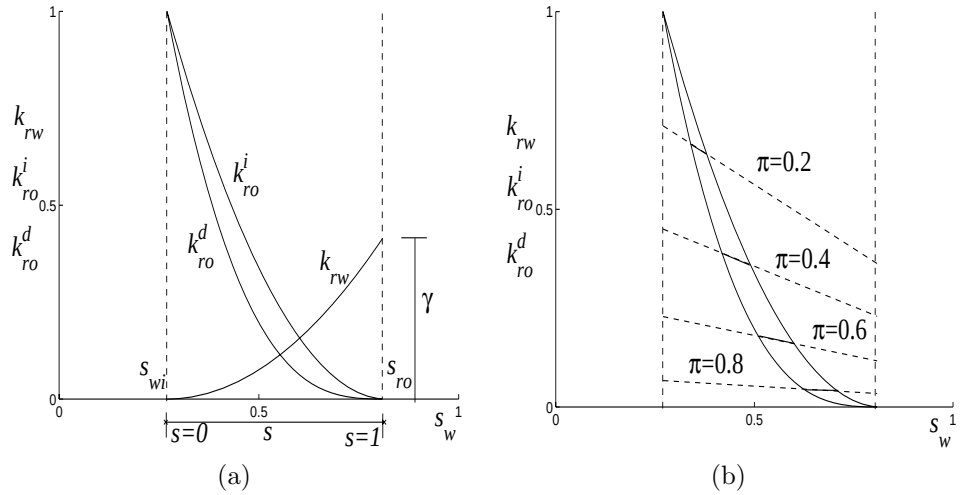

FIG. 2.1. (a) *Nonwetting imbibition and drainage permeabilities functions, and wetting permeability, and* (b) *scanning curves (as a function of the saturation of the wetting phase s_w and the hysteresis parameter π); inspired by Braun and Holland* [6].

where the parameter π ($0 \le \pi \le 1$) discriminates each scanning curve. We use $\xi = 2$ and $\zeta = 1$; therefore, k_{ro} defined above is linear in s for each fixed π; see Figure 2.1(b). Notice that the dashed lines meet at the point $(1/\alpha, 0)$, where α is another parameter used to adjust the slopes of the scanning curves to the experimental ones. We use $\alpha = 0.5$. In the SHM, the scanning curve associated to π is defined in the saturation range $s^i(\pi) < s < s^d(\pi)$. The functions $s^i(\pi)$ and $s^d(\pi)$ are defined implicitly by

$$k^d_{ro}(s^d(\pi)) = k_{ro}(s^d(\pi), \pi) \quad \text{and} \quad k^i_{ro}(s^i(\pi)) = k_{ro}(s^i(\pi), \pi). \tag{2.7}$$

On the drainage and imbibition permeability curves, expressions for the parameter π as a function of the saturation s, and vice versa, can be obtained. Thus we define from (2.7) the functions $\pi^d(s)$ and $\pi^i(s)$. Plots of these functions are shown in Figure 2.2(a).

The flux (2.2) depends on the history (expressed by the parameter π) and the type of the flow (expressed through the sign of $\partial_t s$). Using the relative permeabilities k_{ro} in (2.6) and (2.5), and using k_{rw} in (2.4), the flux function (2.2) takes the form

$$F(s, \pi) \text{ in the scanning region, where } \partial_t \pi = 0, \tag{2.8}$$

$$F^d(s) := F(s, \pi^d(s)) \text{ on the drainage curve, where } \partial_t s < 0, \tag{2.9}$$

$$F^i(s) := F(s, \pi^i(s)) \text{ on the imbibition curve, where } \partial_t s > 0. \tag{2.10}$$

The fluxes $F(s, \pi)$, $F^d(s)$, and $F^i(s)$ (given by (2.2), (2.9), and (2.10), respectively) are shown in Figure 2.2(b). Notice that the drainage and imbibition curves $F^d(s)$ and $F^i(s)$ bound the admissible scanning region Ω on the plane (s, F), defined as $\Omega = \{(s, F) \in \Re^2 : F^d(s) \le F \le F^i(s)\}$. We define the drainage and imbibition curves as $dr := \{(s, F) \in \Re^2 : F = F^d(s)\}$ and $im := \{(s, F) \in \Re^2 : F = F^i(s)\}$, respectively. The permeability functions (2.4) and (2.5) lead to the following necessary properties of the fractional flow function in the scanning, drainage, and imbibition

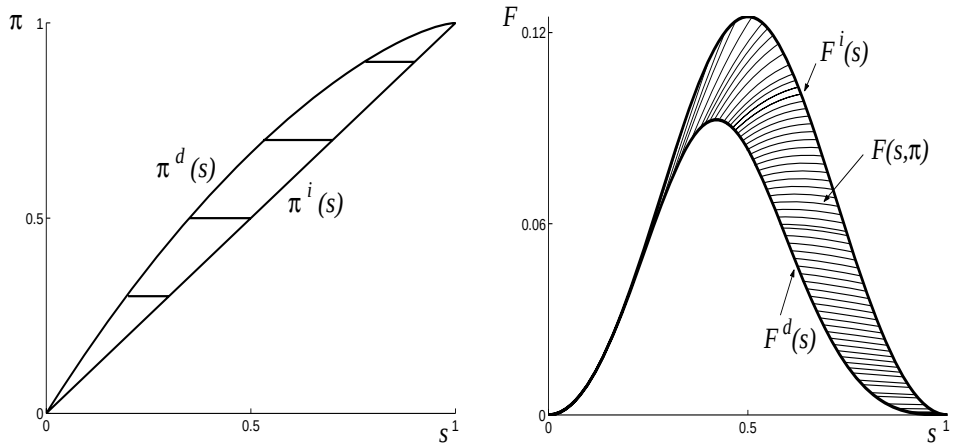

(a) (b)

FIG. 2.2. (a) *State space.* (b) *Fractional flow curves (imbibition, drainage, and scanning).*

flows in the SHM:

$$F^d(0) = 0, \quad F^d(1) = 0, \quad F^i(0) = 0, \quad F^i(1) = 0, \tag{2.11}$$

$$\partial_s F^d(s) \leq \partial_s F(s, \pi^d(s)), \quad \partial_s F^i(s) \leq \partial_s F(s, \pi^i(s)); \tag{2.12}$$

of course other permeability functions satisfying (2.11) and (2.12) can be chosen. These properties ensure that the intersection of the scanning curves with the drainage (or imbibition) curve varies smoothly with π. In addition, as we will see in the next section, property (2.12) guarantees the existence of solution at the intersections of the scanning with the drainage and imbibition curves.

3. The Riemann problem. For imbibition and drainage flows the pair (s, π) lies on the imbibition and drainage curves; therefore the value of π is given by $\pi = \pi^i(s)$ and $\pi = \pi^d(s)$. In these cases, scalar conservation laws are satisfied:

$$\partial_t s + \partial_z F^j(s) = 0, \ j := i, d. \tag{3.1}$$

For scanning flow the conservation law (3.1) is extended to include the independent variable π. Hence the conservation law becomes

$$\partial_t s + \partial_z F(s, \pi) = 0, \tag{3.2}$$

$$\partial_t \pi = 0, \tag{3.3}$$

and can be written in quasi-linear form $\partial_t u + A^s \partial_z u = 0$ with Jacobian

$$A^s = \begin{bmatrix} \partial_s F(s,\pi) & \partial_\pi F(s,\pi) \\ 0 & 0 \end{bmatrix} \text{ and } u := [s, \pi]^T.$$

For scanning flow, the eigenvalues of A^s (or characteristics speeds) are zero and $\partial_s F(s, \pi)$, with corresponding eigenvectors $[\partial_\pi F(s,\pi), \ -\partial_s F(s,\pi)]^T$ and $[1, \ 0]^T$.

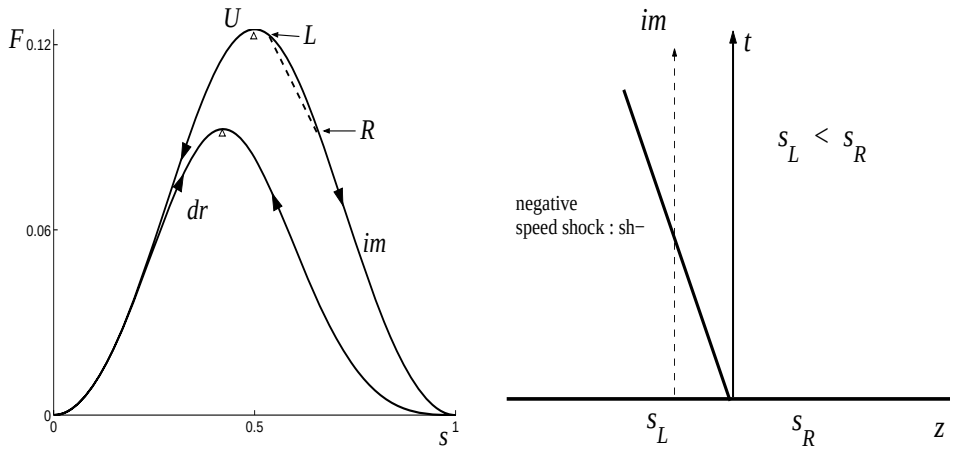

FIG. 3.1. *Flow direction in drainage and imbibition curves. dr: drainage, im: imbibition;* s_U*: saturation associated to the state* $U = \big(s_U, F^i(s_U)\big)$.

3.1. Wave families. For each flow we describe the solution of the Riemann problem:

$$(s,\pi)|_{t=0} = \begin{cases} (s_L, \pi_L) & \text{for } z < z_o, \\ (s_R, \pi_R) & \text{for } z > z_o. \end{cases} \tag{3.4}$$

Hereafter, we will use the following notation. A state L is defined as $L := (s, F) \in \Omega$, where s_L and F_L are the saturation and the flux associated to the state L. Additionally, π_L is the associated parameter π to the state L. In the scanning region, $F_L = F(s_L, \pi_L)$, and on the curve dr (im) $F_L = F^d(s_L)$ $(F_L = F^i(s_L))$.

3.1.1. Imbibition or drainage flow. Since in imbibition (drainage) flow the saturation increases (decreases) in time, i.e., $\partial_t s > 0$ $(\partial_t s < 0)$, a rarefaction wave is characterized by a continuous and monotonically increasing speed $\lambda = \partial_s F^j(s)$ from s_L to s_R. Additionally, a shock wave with speed σ satisfies the Rankine–Hugoniot (RH) condition:

$$\sigma = \frac{F^j(s_R) - F^j(s_L)}{s_R - s_L},\ j = i, d; \tag{3.5}$$

furthermore, the shock is required to satisfy the Oleinik entropy condition for scalar equations. Therefore, admissible sequences of shock and rarefaction waves can be constructed graphically using the concave and convex hull of the fractional flow curves, following [16]. We still have to impose the imbibition and drainage flow orientation. Let s_U be the saturation that maximizes $F^i(s)$ $(U := \{(s_U, F^i(s_U) : F_U = \max(F^i(s)) \text{ for } 0 \le s \le 1\})$. To select the imbibition (drainage) flow orientation the conditions $s_U \le s_L \le s_R$ or $s_R \le s_L \le s_U$ $(s_U \le s_R \le s_L$ or $s_L \le s_R \le s_U)$ must hold. For instance, a shock satisfying these conditions is shown in Figure 3.1(a), and we see that $\partial_t s > 0$ in Figure 3.1(b). For other cases, such as $s_U \le s_R \le s_L$, $s_L \le s_R \le s_U$ $(s_U \le s_L \le s_R$, $s_R \le s_L \le s_U$ for drainage), $s_L \le s_U \le s_R$, and $s_R \le s_U \le s_L$, the Riemann solution must contain scanning waves; otherwise $\partial_t s$ would be negative and therefore the solution could not be on the imbibition curve.

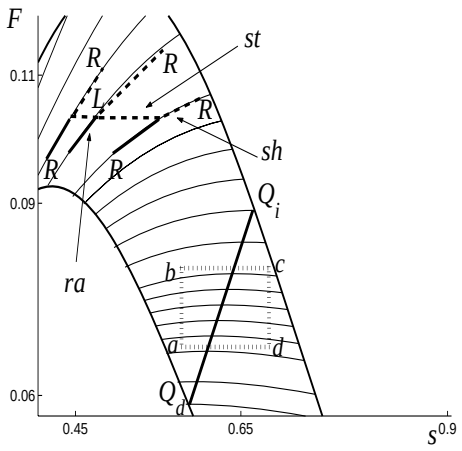

FIG. 3.2. *Scanning cases. Stationary shock, st; shock, sh; rarefaction, ra.*

3.1.2. Scanning flow. The RH condition is

$$F(s_R, \pi_R) - F(s_L, \pi_L) = \sigma(s_R - s_L), \tag{3.6}$$

$$0 - 0 = \sigma(\pi_R - \pi_L). \tag{3.7}$$

Equations (3.6) and (3.7) are satisfied by two kinds of discontinuities; see Figure 3.2. The first one is a shock with speed σ:

$$F(s_R, \pi) - F(s_L, \pi) = \sigma\,(s_R - s_L)\,, \tag{3.8}$$

where π is constant, i.e., $\pi = \pi_L = \pi_R$. This corresponds to the Riemann solution of the single scalar conservation law (3.2) (see Figure 3.2). The second kind of discontinuities satisfying the RH condition (3.6)–(3.7) are stationary discontinuities with speed $\sigma = 0$ and constant fractional flow function; generically they satisfy $\pi_R \neq \pi_L$ and $s_L \neq s_R$.

Summarizing, the scanning curve and the horizontal line through state L divide the scanning region in R-regions where the solution consists of a combination of a stationary wave and scanning waves that are either rarefaction or shocks. Some simple cases are presented in Figure 3.2. A more complex Riemann solution exists when scanning curves have a maximum in Ω and there is no interaction with the imbibition and drainage curves. This RP presents multiplicity of solutions; therefore, we have to make choices to have appropriate solutions. To classify the chosen Riemann solutions, we analyze the *abcd* region in Figure 3.2. This region is sketched in Figures 3.3(a) and (b). The curve Q_dQ_i is the set of states $Q = (s, F(s,\pi))$ in Ω where the saturation s maximizes $F(s,\pi)$ for each π (see Figure 3.2).

In Figures 3.3(a) and (b), we show the regions and their associated Riemann solutions for left states L_1 and L_2 lying on opposite sides of the curve Q_dQ_i. A summary of the solutions is given in Table 3.1; the waves are ordered from lower to higher speeds. For example, the solution $L_1I_1R_1$ consists of a stationary shock L_1I_1 connecting states L_1 and I_1 (denoted by $L_1 \xrightarrow{st} I_1$), and a positive speed shock I_1R_1 connecting states I_1 and R_1 (denoted by $I_1 \xrightarrow{sh+} R_1$).

3.1.3. Intermediate flow. Denoting by I the intersection state between the π_L-scanning and the drainage (imbibition) curves, the solution between a scanning state

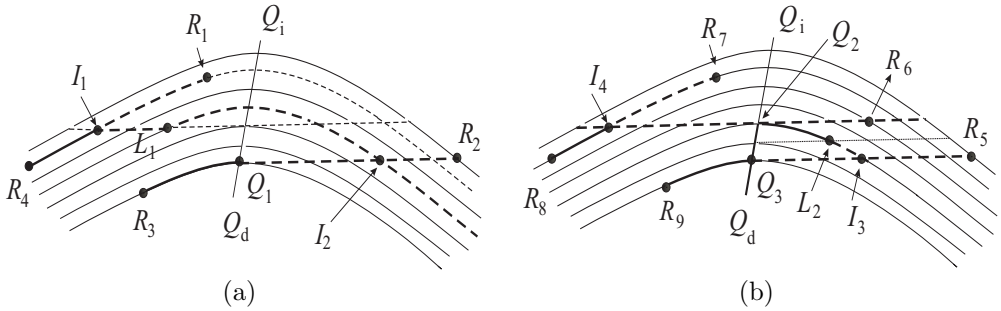

FIG. 3.3. *Regions in the scanning region abcd of Figure* 3.2.

TABLE 3.1

Riemann solutions for a region where the scanning curves have a maximum in Ω *where waves are ordered from negative to positive. Negative speed rarefaction:* $ra-$*, negative speed shock:* $sh-$*, stationary shock:* st*, positive speed rarefaction:* $ra+$*, and positive speed shock:* $sh+$*.*

Riemann solutions for L_1, Figure 3.3(a)
waves
$L_1 \xrightarrow{st} I_1 \xrightarrow{sh+} R_1$
$L_1 \xrightarrow{sh-} I_2 \xrightarrow{st} R_2$
$L_1 \xrightarrow{sh-} I_2 \xrightarrow{st} Q_1 \xrightarrow{ra+} R_3$
$L_1 \xrightarrow{st} I_1 \xrightarrow{ra+} R_4$
Riemann solutions for L_2, Figure 3.3(b)
waves
$L_2 \xrightarrow{sh-} I_3 \xrightarrow{st} R_5$
$L_2 \xrightarrow{ra-} Q_2 \xrightarrow{st} R_6$
$L_2 \xrightarrow{ra-} Q_2 \xrightarrow{st} I_4 \xrightarrow{sh+} R_7$
$L_2 \xrightarrow{ra-} Q_2 \xrightarrow{st} I_4 \xrightarrow{ra+} R_8$
$L_2 \xrightarrow{sh-} I_3 \xrightarrow{st} Q_3 \xrightarrow{ra+} R_9$

L and a drainage (imbibition) state R is constructed using a concave (convex) hull curve on the effective flux function LIR (see Figure 3.4). Therefore, the interaction of the two waves LI and IR yields a shock LR with speed

$$\sigma = \frac{F^d(s_R) - F(s_L, \pi_L)}{s_R - s_L}, \tag{3.9}$$

since the shock IR has a smaller speed than the rarefaction LI, i.e., $(F^d(s_R) - F^d(s^d(\pi_L)))/(s_R - s^d(\pi_L)) \le \partial_s F(s^d(\pi_L), \pi_L)$, and at I the drainage and scanning curves satisfy inequalities (2.12).

3.2. Riemann solutions. The construction of the Riemann solutions is simplified by describing state space in terms of (s, F) instead of (s, π). We subdivide Ω into four subregions (L-regions) defined as follows (see Figure 3.5):

$$\begin{aligned}
A &= \{(s,F) \in \Omega : s_{Q_d} \le s \le 1 \text{ and } F \le F(s, \pi_{Q_d})\},\\
B &= \{(s,F) \in \Omega : s_M \le s \le s_P \text{ and } F(s, \pi_{Q_d}) \le F \le F^d(s_M)\},\\
C &= \{(s,F) \in \Omega : 0 \le s \le 1 \text{ and } F^d(s_M) \le F\},\\
D &= \{(s,F) \in \Omega : 0 \le s \le s_M \text{ and } F \le F^d(s_M)\},
\end{aligned}$$

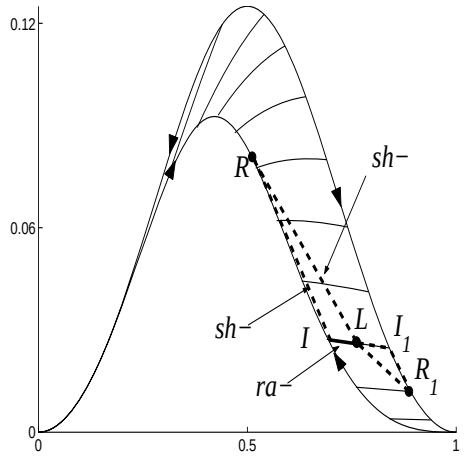

(a)

FIG. 3.4. *Transition from a scanning curve to a drainage or imbibition curve.*

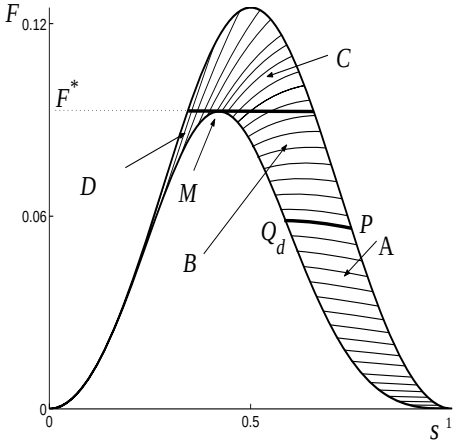

FIG. 3.5. *L-regions of* Ω.

where the imbibition state P is defined as the intersection point of the imbibition curve with the scanning curve through the states Q_d, while M is the state where s_M maximizes $F^d(s_M)$. Next we construct the solutions for L in each of the L-regions.

Case A: $L_1 = (s_L, F(s_L, \pi_L)) \in A$. In this case, there are the following six R-regions (see Figure 3.6(a)):

$$\begin{aligned}
\Re_A^I &= \{(s,F) \in \Omega : s_E \le s \text{ and } F \le F(s,\pi_L)\},\\
\Re_A^{II} &= \{(s,F) \in \text{region enclosed by } EKVQ_d\},\\
\Re_A^{III} &= \{(s,F) \in \text{region enclosed by } Q_dVGT\},\\
\Re_A^{IV} &= \{(s,F) \in \Omega : s_M \le s \le s_G \text{ and } F(s,\pi_T) \le F \le F(s,\pi_M)\},\\
\Re_A^{V} &= \{(s,F) \in \Omega : s_H \le s \le s_N \text{ and } F(s,\pi_M) \le F \text{ and } F^d(s_M) \le F\},\\
\Re_A^{VI} &= \{(s,F) \in \Omega : s \le s_M \text{ and } F \le F^d(s_M)\},
\end{aligned}$$

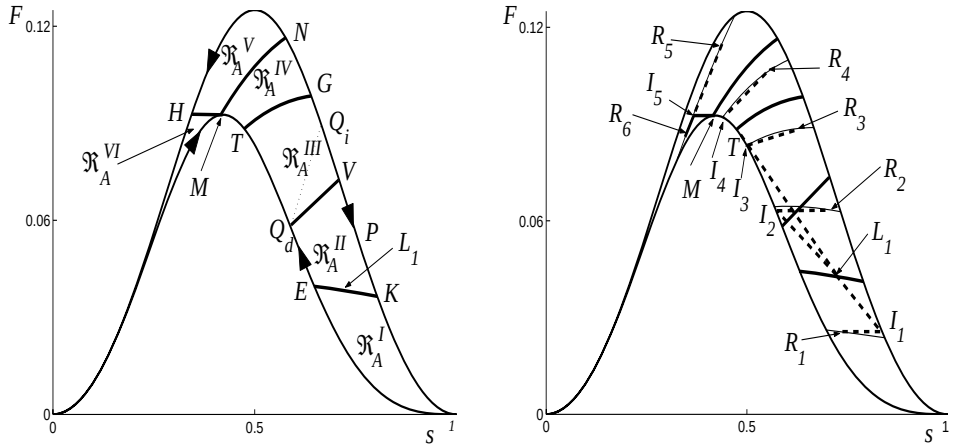

(a) (b)

FIG. 3.6. *Figure* (a) *(Case A): R-regions for L_1 in L-region A. Figure* (b) *(Case A): solutions for L_1 in L-region A and R in R-regions: $R_1 \in \Re_A^I$, $R_2 \in \Re_A^{II}$, $R_3 \in \Re_A^{III}$, $R_4 \in \Re_A^{IV}$, $R_5 \in \Re_A^V$, and $R_6 \in \Re_A^{VI}$.*

where the states E and K are the intersection of drainage and imbibition curves with the scanning curve through L_1. We define the state $V \in im$ and the curve Q_dV by $Q_dV := \{W = (s_W, F_W) \in \Omega : (s_W, F_W) = (s_I + 2(s_Q - s_I), F_I)\ \forall I \in dr\}$. States N and H are the intersections of the imbibition curve with the scanning and the horizontal line through M, respectively. We define the drainage state T through $\partial_s F^d(s_T) = (F^d(s_T) - F_L)/(s_T - s_L)$, and the state G as the intersection of the imbibition curve with the scanning curve though T. Notice that T and G depend on L_1. Assuming that $\partial_{ss}F(s,\pi) < 0$, the Riemann solution associated to each R-region as shown in Figure 3.6(a) is presented in Figure 3.6(b) and described below:

A.1. For $R_1 \in \Re_A^I$, the solution is $L_1 \xrightarrow{sh-} I_1 \xrightarrow{st} R_1$.

A.2. For $R_2 \in \Re_A^{II}$, the solution is $L_1 \xrightarrow{sh-} I_2 \xrightarrow{st} R_2$.

A.3. For $R_3 \in \Re_A^{III}$, the solution is $L_1 \xrightarrow{sh-} I_3 \xrightarrow{sh+} R_3$, where state I_3 is determined by the intersection of the drainage curve with the scanning curve through R_3.

A.4. For $R_4 \in \Re_A^{IV}$, the solution is $L_1 \xrightarrow{sh-} T \xrightarrow{ra-} I_4 \xrightarrow{sh+} R_4$, where I_4 is determined by the intersection of the drainage curve with the scanning curve through R_4.

A.5. For $R_5 \in \Re_A^V$, the solution is $L_1 \xrightarrow{sh-} T \xrightarrow{ra-} M \xrightarrow{st} I_5 \xrightarrow{sh+} R_5$, where state I_5 is the intersection of the horizontal line through M and the scanning curve through R_5.

A.6. For $R_6 \in \Re_A^{VI}$, the solution is $L_1 \xrightarrow{sh-} T \xrightarrow{ra-} M \xrightarrow{st} I_5 \xrightarrow{ra+} R_6$. When I_5 is on the imbibition curve, the solution will be shown in Case *C*, Figure 3.9(a)

Case B: $L_2 = (s_L, F(s_L, \pi_L)) \in B$. The R-regions are shown in Figure 3.7(a). The Riemann solutions for the R-regions $\Re_B^V$, $\Re_B^{VI}$, and $\Re_B^{VII}$ are analogous to those of solutions for the R-regions $\Re_A^{IV}$, $\Re_A^V$, and $\Re_A^{VI}$, respectively. The solutions for R-regions $\Re_B^I$, $\Re_B^{II}$, $\Re_B^{III}$, and $\Re_B^{IV}$ are shown in Figure 3.7(b) and described below:

B.1. For $R_1 \in \Re_B^I$, the solution is $L_2 \xrightarrow{sh-} I_1 \xrightarrow{st} R_1$.

B.2. For $R_2 \in \Re_B^{II}$, the solutions is $L_2 \xrightarrow{sh-} I_2 \xrightarrow{st} Q \xrightarrow{ra+} R_2$.

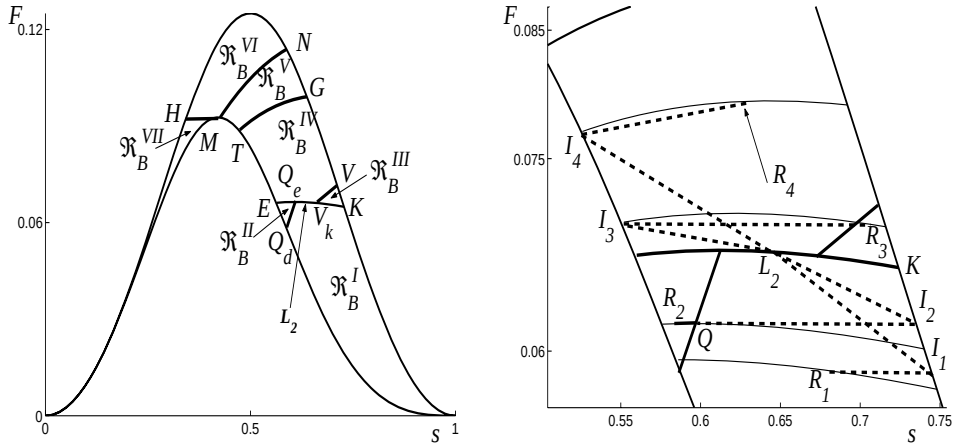

FIG. 3.7. *Figure* (a) *(Case B): R-regions for L_2 in the L-region B. Figure* (b) *(Case B): L_2 in L-region B and $R_1 \in \Re_B^I$, $R_2 \in \Re_B^{II}$, $R_2 \in \Re_B^{III}$, and $R_4 \in \Re_B^{IV}$.*

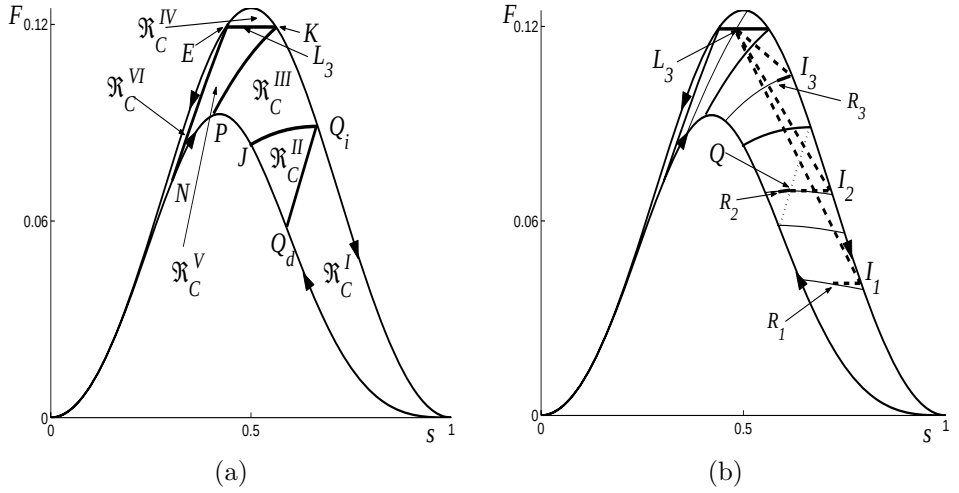

FIG. 3.8. *Figure* (a) *(Case C): R-regions for L_3 in L-region C. Figure* (b) *(Case C): solutions for L_3 in L-region C and R in R-regions: $R_1 \in \Re_C^I$, $R_2 \in \Re_C^{II}$, and $R_3 \in \Re_C^{III}$.*

B.3. For $R_3 \in \Re_B^{III}$, the solution is $L_2 \xrightarrow{sh-} I_3 \xrightarrow{st} R_3$.

B.4. For $R_4 \in \Re_B^{IV}$, the solution is $L_2 \xrightarrow{sh-} I_4 \xrightarrow{sh+} R_4$.

Case C: $L_3 = (s_L, F(s_L, \pi_L)) \in C$. The R-regions are shown in Figure 3.8(a). The Riemann solution belongs to one of the following cases:

C.1. For $R_1 \in \Re_C^I$ (Figure 3.8(b)), the solution is $L_3 \xrightarrow{sh-} I_1 \xrightarrow{st} R_1$.

C.2. For $R_2 \in \Re_C^{II}$, the solution is analogous to that of Case B (subcase B.2). In the solution shown, I_2 cannot be connected to R_2 only by a stationary shock because the stationary shock intersects the scanning curve with π_R. Therefore, the solution is $L_3 \xrightarrow{sh-} I_2 \xrightarrow{st} Q \xrightarrow{ra+} R_2$.

C.3. For $R_3 \in \Re_C^{III}$, the solution is $L_3 \xrightarrow{sh-} I_3 \xrightarrow{ra+} R_3$.

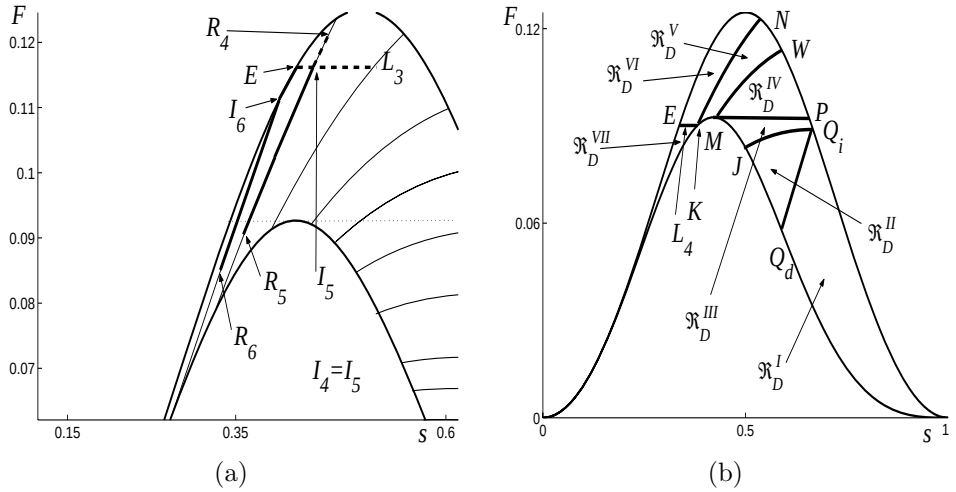

FIG. 3.9. *Figure* (a) *(Case C): solutions for* $L_3 \in C$ *and* R *in* R*-regions:* $R_5 \in \Re_C^V$ *and* $R_6 \in \Re_C^{VI}$. *Figure* (b) *(Case D): R-regions for* $L_4 \in D$.

C.4. For $R_4 \in \Re_C^{IV}$ (Figure 3.9(a)), the solution is $L_3 \xrightarrow{st} I_5 \xrightarrow{sh+} R_4$.

C.4. For $R_5 \in \Re_C^V$, the solution is $L_3 \xrightarrow{st} I_5 \xrightarrow{ra+} R_5$.

C.5. For $R_6 \in \Re_C^{VI}$, L_3 cannot be connected to the scanning curve through R_6 only by a stationary shock, because the latter intersects the imbibition curve (state E). For L_3 and R_6 the solution is $L_3 \xrightarrow{st} E \xrightarrow{ra+} I_6 \xrightarrow{ra+} R_6$.

Case D: $L_4 = (s_L, F(s_L, \pi_L)) \in D$. The R-regions are shown in Figure 3.9(b). The Riemann solutions belong to one of the following cases:

D.1. For $R_1 \in \Re_D^I$ (Figure 3.10(a)), the solution is $L_4 \xrightarrow{st} K \xrightarrow{sh-} I_2 \xrightarrow{st} R_1$.

D.2. For $R_2 \in \Re_D^{II}$, the solution is $L_4 \xrightarrow{st} K \xrightarrow{sh-} I_1 \xrightarrow{st} Q \xrightarrow{ra} R_2$.

D.3. For $R_3 \in \Re_D^{III}$, the solution is $L_4 \xrightarrow{st} K \xrightarrow{sh+} I_3 \xrightarrow{ra+} R_3$. Notice that segment KI_3 is tangent to the *dr* curve at I_3 to the scanning curve through R_3.

D.4. For $R_4 \in \Re_D^{IV}$, the solution is $L_4 \xrightarrow{st} K \xrightarrow{sh+} I_4 \xrightarrow{sh+} R_4$.

D.5. For $R_5 \in \Re_D^{IV}$ (Figure 3.10(b)), the solution is $L_4 \xrightarrow{st} K \xrightarrow{sh+} I_5 \xrightarrow{sh+} R_5$.

D.6. For $R_6 \in \Re_D^{VI}$, the solution is $L_4 \xrightarrow{st} I_6 \xrightarrow{sh+} R_6$.

D.7. For $R_7 \in \Re_D^{VII}$, the solution is $L_4 \xrightarrow{st} I_7 \xrightarrow{ra+} R_7$. If the stationary shock intersects the *im* curve, the solution is analogous to that of Case C (subcase C.5).

3.3. Uniqueness criteria. Without appropriate restrictions for given L and R states, the Riemann problem might have multiple solutions. We are interested in solutions satisfying (1) the Oleinik condition in Ω and (2) the orientation of the drainage and imbibition curves. However, these conditions are insufficient to guarantee uniqueness of solution. A solution can be obtained if we further require that (3) the solution must be $\mathcal{L}_1^{loc}$ continuous with respect to changes in L and R. A Riemann solution is well posed if it satisfies conditions (1), (2), and (3) mentioned above. The choices presented in section 3.2 give rise to well-posed global solutions; however, some of them are not evident; so we discuss these cases here.

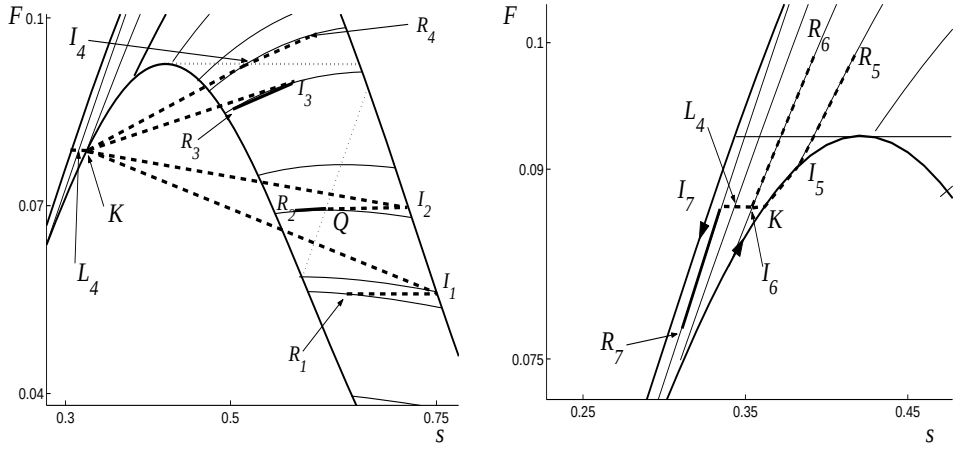

FIG. 3.10. *Figure* (a) *(Case D): L_4 in L-region D and R in R-regions $R_3 \in \Re^{III}$, $R_4 \in \Re^{IV}$, $R_5 \in \Re^{V}$, and $R_6 \in \Re^{VI}$. Figure* (b) *(Case D): $L_4 \in D$ and R in R-regions $R_1 \in \Re^{I}$ and $R_2 \in \Re^{II}$.*

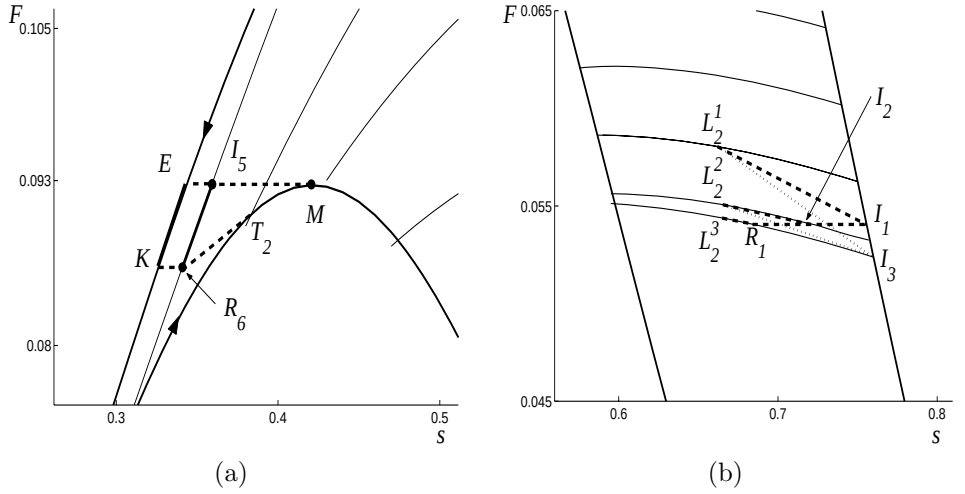

FIG. 3.11. *Figure* (a) *(Case A): $R_6 \in \Re_A^{VI}$. Figure* (b) *(Case B): $L_2^1 \in B$ and $R_1 \in \Re_B^I$.*

Case A: $L_1 \in A$ and $R_6 \in \Re_A^{VI}$. As mentioned in section 3.2, the solution for this case is represented by the segment $L_1TMI_5R_6$ as shown in Figure 3.6(b). We show that other tentative solutions are impossible. In Figure 3.11(a) we analyze the connection between states M and R_6. Consider the curve MT_2R_6: the rarefaction MT_2 and shock T_2R_6. This solution is inadmissible because the rarefaction MT_2 violates the physical orientation of the drainage curve. Another tentative solution such as $MEKR_6$ is also inadmissible because the interaction of the waves EK and KR_6 yields the shock ER_6, which violates the scanning region RH condition (3.6), (3.7). Therefore, between states M and R_6, the sequence $LTMIR_6$ is the only admissible solution that we were able to find.

Case B: $L_2^1 \in B$ and $R_1 \in \Re_B^I$ (see Figure 3.7(b)). We choose the Riemann solution $L_2^1I_1R_1$. We can also consider $L_2^1I_3R_1$ as another solution (see Figure 3.11(b)).

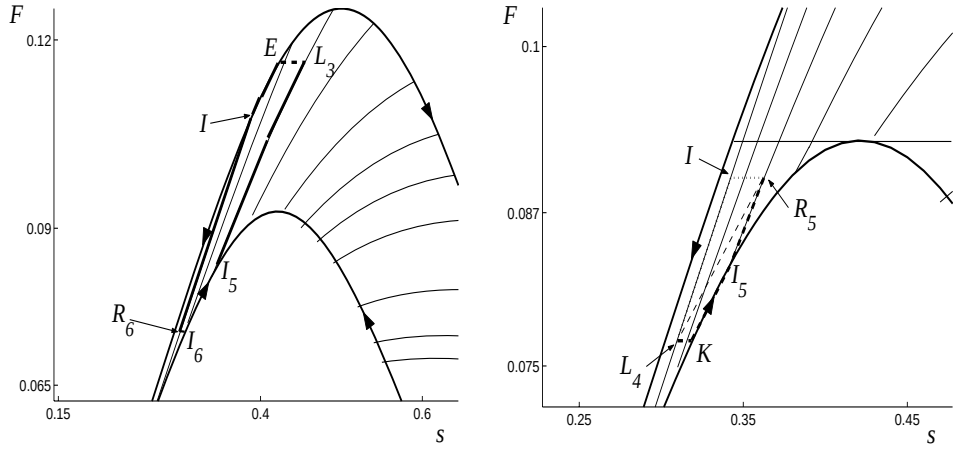

(a) (b)

FIG. 3.12. *Figure* (a) *(Case C): $L_3 \in C$ and $R_6 \in \Re_C^{VI}$. Figure* (b) *(Case D): $L_4 \in D$ and $R_5 \in \Re_D^V$.*

In principle $L_2^1 I_1 R_1$ and $L_2^1 I_3 R_1$ seem possible. However, only the solution $L_2^1 I_1 R_1$ depends continuously on changes of the left and right states. To analyze these solutions we change the state L_2^1. In this case the solution $L_2^1 I_3 R_1$ generates a sequence of solutions

$$L_2^1 I_3 R_1 \to L_2^2 I_3 R_1 \to L_2^3 I_3 R_1, \tag{3.10}$$

which converges to the wrong solution $L_2^3 I_3 R_1$. Notice that when $L_2^1 = L_2^3$ the correct solution is a shock $L_2^3 R_1$. Additionally, the solution $L_2^1 I_1 R_1$ generates a sequence of solutions

$$L_2^1 I_1 R_1 \to L_2^2 I_2 R_1 \to L_2^3 R_1 \tag{3.11}$$

converging to the correct solution $L_2^3 R_1$ without producing $\mathcal{L}_1^{loc}$ discontinuities in the Riemann solution. Therefore, solutions other than $L_2^1 I_1 R_1$ do not ensure the continuity of the solution when the states L and R are perturbed.

Case C: $L_3 \in C$ and $R_6 \in \Re_C^{VI}$. In this case the orientation of the drainage and imbibition curves ensures the uniqueness and $\mathcal{L}_1^{loc}$ continuity of the Riemann solution. For example, in Figure 3.12(a), the solution for left and right states L_3 and R_6 is $L_3 E I R_6$; notice that another tentative solution such as $L_3 I_5 I_6 R_6$ is inadmissible because the rarefaction $I_5 I_6$ violates the drainage curve orientation.

Case D: $L_4 \in D$ and $R_5 \in \Re_D^V$. From Figure 3.12(b), the solution chosen is $L_4 K I_5 R_5$. A tentative solution such as $L_4 I R_5$ is not possible because its yields a shock $L_4 R_5$ which violates the scanning region Oleinik condition.

4. The corrected Godunov method. We discretize the z-t plane by choosing a mesh width $h := \Delta z = 1/N_z$ and a time step $k = \Delta t$, and we define the discrete grid points (z_j, t_n) by

$$z_j = jh + h/2,\ z_{j\pm 1/2} = z_j \pm h/2,\ \ j = 0, 1, 2, \ldots, N_z - 1, \tag{4.1}$$

$$t_n = nk,\ \ n = 0, 1, 2, \ldots . \tag{4.2}$$

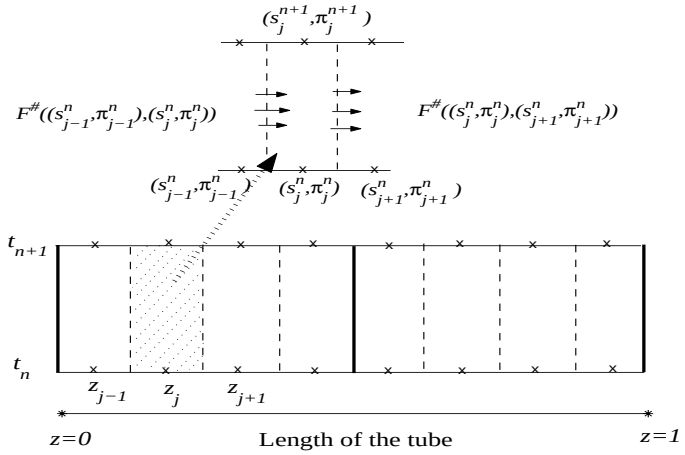

FIG. 4.1. *Numerical fluxes using local Riemann solution.*

Each time step of the numerical method consists of two stages. In the first stage (*predictor*) equations (3.1) and (3.2) are solved numerically by the Godunov method [11]. The second stage (*corrector*) is the correction of the parameter π, which is necessary when the predicted state lies outside the admissible region Ω. In such a case, the corrected state is obtained from the predicted state by a projection (with fixed s) on $\partial\Omega$ of the predictor state. The saturation is maintained constant in order to preserve conservation of mass, which is guaranteed in the prediction step because it uses Godunov method.

Predictor. Denoting the cell state at (z_j, t_n) by (s_j^n, π_j^n), we then have that the conservative Godunov method on a cell $[z_{j-1/2}, z_{j+1/2}] \times [t_n, t_{n+1}]$ for the saturation value is expressed as

$$s_j^{n+1} = s_j^n - \frac{k}{h}[F^{\#}((s_j^n,\pi_j^n),(s_{j+1}^n,\pi_{j+1}^n)) - F^{\#}((s_{j-1}^n,\pi_{j-1}^n),(s_j^n,\pi_j^n))], \tag{4.3}$$

where $F^{\#}((s_j^n,\pi_j^n),(s_{j+1}^n,\pi_{j+1}^n))$ and $F^{\#}((s_{j-1}^n,\pi_{j-1}^n),(s_j^n,\pi_j^n))$ are the numerical fluxes at the right and left boundaries of the cell $[z_{j-1/2}, z_{j+1/2}] \times [t_n, t_{n+1}]$, respectively. We impose zero numerical flux boundary conditions at $z = 0$ and $z = 1$; see Figure 4.1.

Notice that the left and right numerical fluxes of each cell are constant along the left and right boundaries, respectively. This is so because these boundaries coincide with zero speed characteristics at $z_{j-1/2}$ and $z_{j+1/2}$, respectively. Consequently, for each pair of states (s, π), the numerical fluxes can be determined directly from the Riemann solution presented in section 3.2.

For example, consider the left state $L = (s_L, F_L)$ and right state $R = (s_R, F_R)$ at time t_n (see Figure 4.1), with the Riemann solution represented in Figure 5.1(b). Then the numerical flux $F^{\#}((s_L^n,\pi_L^n),(s_R^n,\pi_R^n))$ is exactly the flux F_M^d specified by the state M or I; notice that either choice produces the same numerical flux as shown in Figure 5.1(b). As another example, consider the left state L and right state R, and suppose that the Riemann solution consists of a positive speed shock represented in Figure 3.10(b) by $L_4KI_5R_5$. Consequently, the numerical flux $F^{\#}((s_L^n,\pi_L^n),(s_R^n,\pi_R^n))$ is $F(s_L, \pi_L)$ at state L_4. In this way, the numerical flux for each pair of left and right states is chosen by using the solutions presented in section 3.2.

Corrector. Once (4.3) for the saturation is satisfied, we update π_j^n. We de-

fine the external imbibition and drainage regions as $\Omega^i := \{(s,F) \in \Re^2 : 0 \le s \le 1 \text{ and } F^i(s) \le F\}$ and $\Omega^d := \{(s,F) \in \Re^2 : 0 \le s \le 1 \text{ and } F \le F^d(s)\}$, respectively. To obtain π_j^{n+1}, we choose $\pi_j^{n+1} = \pi_j^n$ if (s_j^{n+1}, π_j^n) lies in the scanning region Ω, and $\pi_j^{n+1} = \pi^i(s_j^{n+1})$ or $\pi_j^{n+1} = \pi^d(s_j^{n+1})$ if $(s_j^{n+1}, F(s_j^{n+1}, \pi_j^n))$ lies on the external imbibition or drainage region, respectively. This strategy for updating π was proposed in [18] and guarantees mass conservation of each phase. For the computational results presented in section 5, we adopt the global CFL condition as $|\frac{k}{h} v_{\max}| \le 1$, where

$$v_{\max} = \max\left(\max_{(s,\pi)\in\Omega} \mid \partial_s F(s,\pi) \mid, \max_{(s,F)\in j} \mid \partial_s F^j(s) \mid\right), \; j = i, d. \tag{4.4}$$

We note, however, that a sharper time-dependent CFL condition can be derived as the maximum velocity of all local Riemann solutions in each time step.

5. Computational results.

Example 1: Comparison between the numerical and the analytical solutions. The aim of this comparison is to demonstrate that the numerical method can capture accurately all the features of the analytical solution. We consider the numerical and analytical dimensionless solutions associated to the Riemann problem with initial discontinuity at $z = 0.50$ separating states $(s_l, \pi_l) = (0.7, 0.8)$ and $(s_r, \pi_r) = (0.3, 0.4)$. Both states lie inside the scanning region. The following parameters were used in the simulations $\mu_w = 1\ cp$, $\mu_o = 0.9\ cp$, and for this case the global CFL condition is 0.3849. The dimensionless simulated time was $t = 2.4\ 10^3$. The analytical solution (represented in Figure 5.1(b)) is shown as a solid line in Figure 5.1(a), and the numerical solution obtained with the proposed scheme using $N_z = 100$ as a dashed line in the same figure.

The numerical and analytical profiles at dimensionless time are presented in Figure 5.1. The saturation profile consists from left to right of a scanning to drainage shock wave LT, followed by a rarefaction wave TM, a stationary wave MI, and a rarefaction wave IR. The small discrepancy around the shock LT in Figure 5.1(a) is due to the correction scheme for π. However, the discrepancy potentially occurs at only one mesh point.

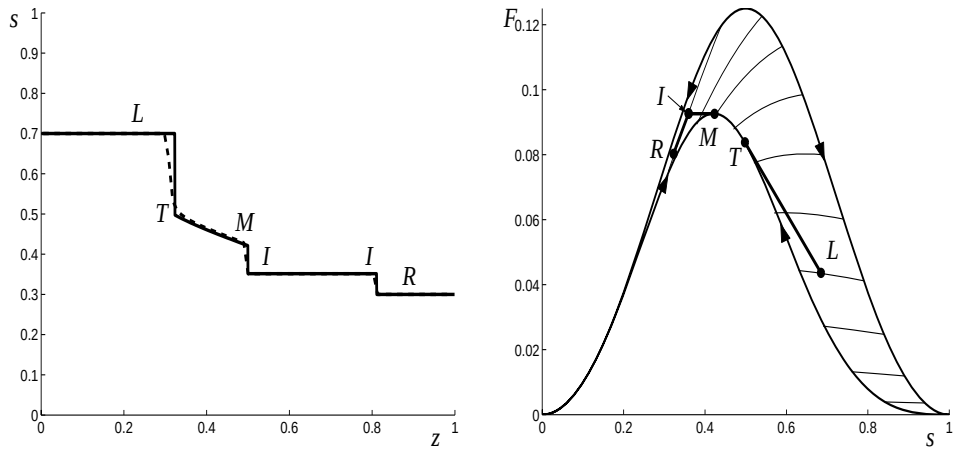

(a) (b)

FIG. 5.1. *Comparison between the analytical and the numerical method. Dashed line corresponds to the numerical solution, and solid corresponds to analytical solution.*

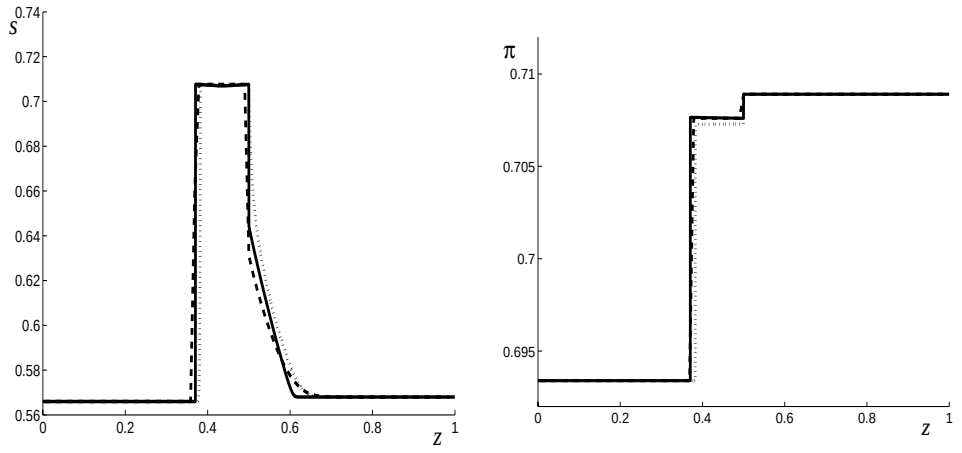

(a) (b)

FIG. 5.2. *The solid curve corresponds to the analytical solution, the dashed curve to the corrected Godunov method with* $N_z = 50$, *and the dotted curve to the corrected Lax–Friedrichs scheme with* $N_z = 4000$. (a) *Saturation values and* (b) π *values.*

Example 2: Comparison between corrected Godunov and corrected Lax–Friedrichs schemes. We consider the Riemann problem with initial discontinuity at $z = 0.50$ separating states $(s_l, \pi_l) = (0.57, 0.69)$ and $(s_r, \pi_r) = (0.57, 0.71)$. Figure 5.2(a) and (b) show a comparison among the proposed corrected Godunov scheme with $N_z = 40$, the corrected Lax–Friedrichs with $N_z = 4000$, and the analytical solution. The global CFL restriction is followed. To obtain an accurate approximation for the analytical solution, the corrected Godunov scheme requires a mesh size $N_z = 40$, while the corrected Lax–Friedrichs requires $N_z = 4000$. Hence, to satisfy the global CFL condition (4.4), the corrected Godunov scheme requires substantially fewer time steps than the corrected Lax–Friedrichs, so that the simulation using the Godunov scheme takes 500 times less CPU time than using the Lax–Friedrichs scheme.

The classical Godunov and Lax–Friedrichs schemes do not work without the corrector step. We note also that the design of numerical schemes for the problems considered here is not trivial. Because of hysteresis, there are stationary waves, the orientation of the curves (imbibition and drainage) has to be taken into account, and the restriction on the admissibility scanning region Ω must be followed.

Example 3: Comparison between solutions with and without hysteresis. The strong influence of the hysteresis effect in the saturation profiles can be seen by comparing the profiles obtained numerically with and without hysteretic relative permeabilities. We choose the drainage curve opposite the imbibition curve as the nonhysteretic relative permeability curve since the corresponding nonhysteretic solution agrees most with the hysteretic solution.

We introduce in the simulation the top and bottom boundaries of the tube. We perform the simulation with $N_z = 50$, $\mu_w = 1$ *cp*, and $\mu_o = 0.9$ *cp*. The density of the wetting phase is $\rho_w = 1$ g/cm^3 and the density of the nonwetting phase is taken as $\rho_o = 0.844$ g/cm^3. We consider the porous media having a permeability of 11.84 Darcys and porosity of 0.389. The tube length is 86 cm. Additionally, $s_L = 0.9$ and $s_R = 0.1$.

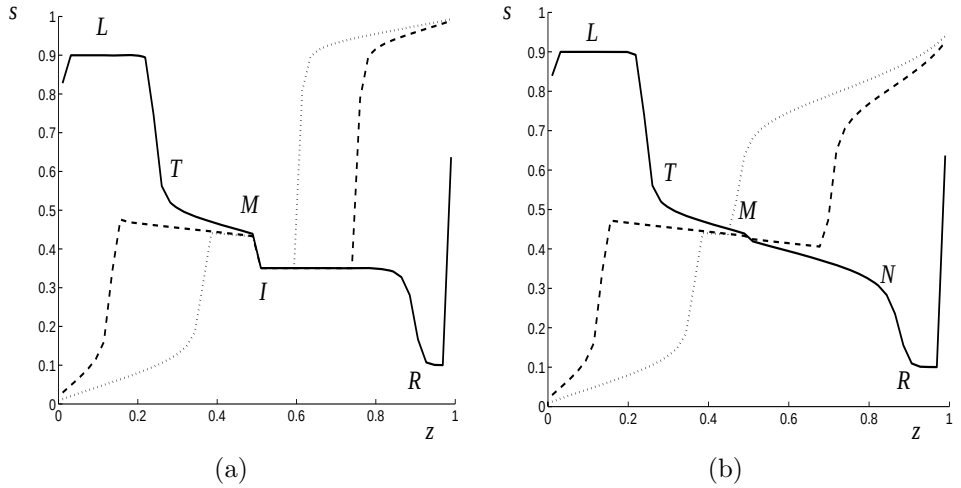

FIG. 5.3. *Profile $s(z)$ at several times:* (a) *hysteretic solution,* (b) *nonhysteretic solution. Saturations are represented as a solid curve at* 5.87 h*, as a dashed curve at* 14.59 h*, and as a dotted curve at* 19.38 h*. Compare with Figure* 5.4.

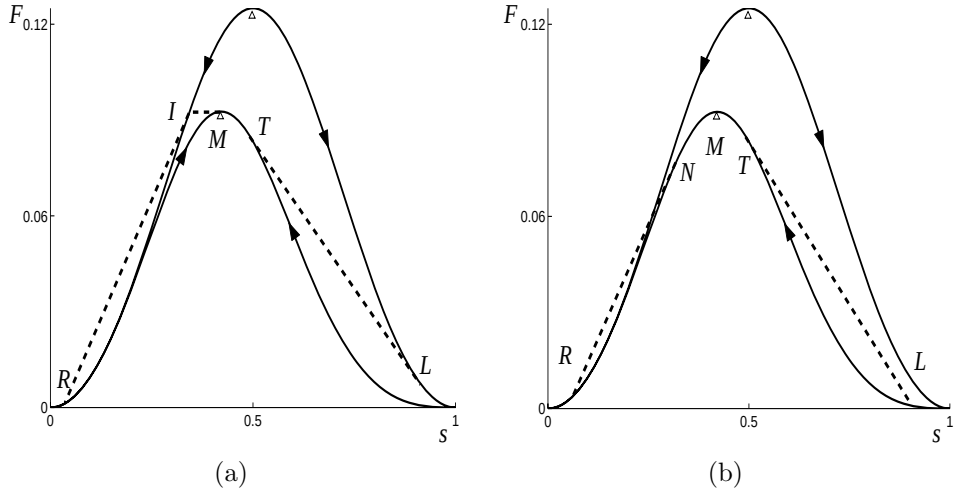

FIG. 5.4. *Solutions in (s, F) space* (a) *with hysteresis,* (b) *without hysteresis at imbibition and drainage curves.*

The hysteretic and nonhysteretic simulation results differ significantly; see Figure 5.3. Observing Figure 5.3(a), three sections are clearly identified. We can see that in the top zone (around $z = 0$), wetting phase saturation decreases with time, i.e., a drainage process. At the bottom zone (around $z = 1$), the saturation increases with time, i.e., an imbibition process. The most relevant discrepancy between hysteretic and nonhysteretic solutions occurs at the middle zone ($z \in [0.3, 0.7]$), where both drainage and imbibition take place. In this zone the hysteretic profiles have a sharper decline MI, which is not captured in Figure 5.3(b) without hysteresis.

The discrepancy between the hysteretic and nonhysteretic solutions can be under-

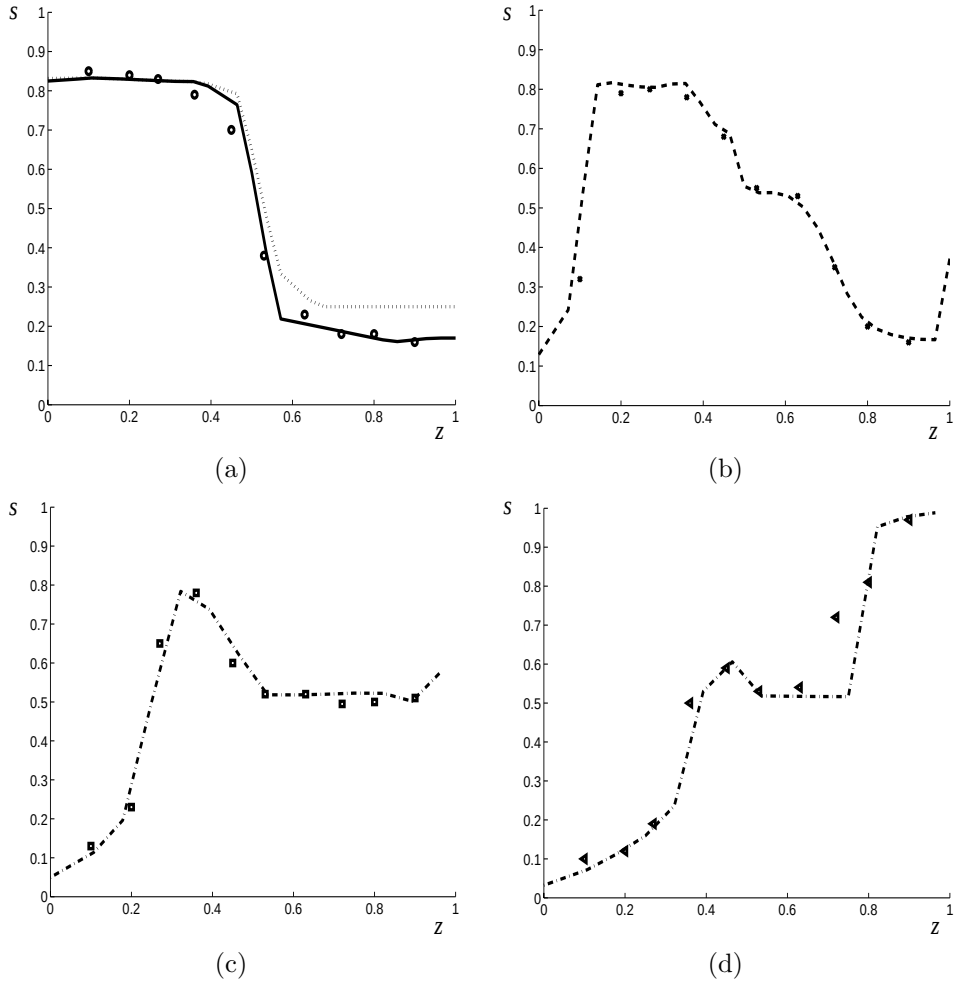

FIG. 5.5. *Comparison between saturation profiles obtained by the numerical simulation and the laboratory data (marked points) several times (*(a) 0 *min.,* (b) 19 *min.,* (c) 60 *min.,* (d) 38.6 *hours). In* (a)*, the dotted line is the initial value of* π *used for the simulation.*

stood by comparing the Riemann solution for hysteretic and nonhysteretic fractional flow functions. With hysteresis (Figure 5.4(a)), the solution combining imbibition and drainage necessarily goes through the scanning region. For instance, consider the case when $s_L > s_R$. Due to the imbibition and drainage curve orientation, the solution is $LTMIR$, a negative speed shock LT, a drainage rarefaction TM, a stationary shock wave MI connecting the drainage and the imbibition curves, and a positive speed imbibition shock IR. On the other hand, without hysteresis (Figure 5.4(b)), the solution is $LTNR$, a negative speed shock LT, a rarefaction wave TN, and a positive speed shock NR.

Example 4: Comparison with experimental work data. To validate the proposed model we compare the numerical gas-water saturation profile with saturation profiles found in [7] and [20]. Following [7], we consider a sand pack with a permeability of 11.84 Darcys and porosity of 0.389. The tube length is 86 cm. Additionally,

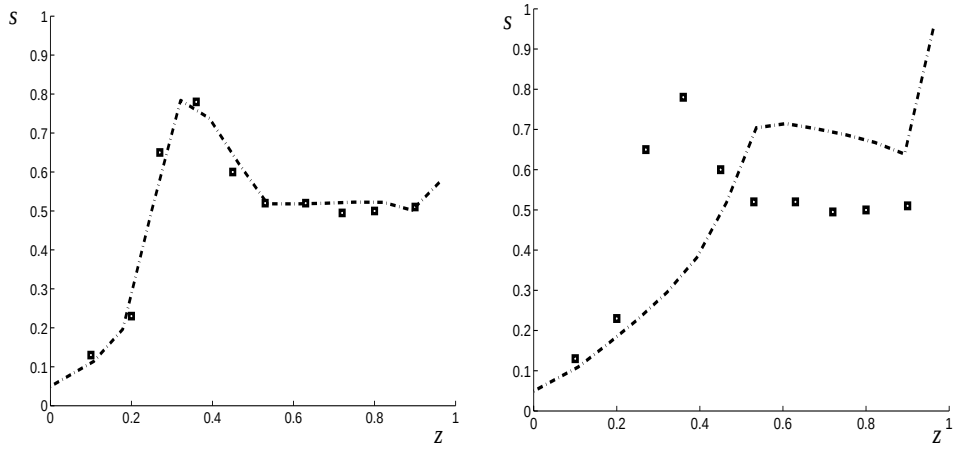

FIG. 5.6. *Comparison between saturation profiles with hysteresis* (a) *and without hysteresis* (b) *obtained by the numerical simulation and the laboratory data (marked points) for* 60 *min.*

we use the following values for the parameters: $\alpha = 0.5$, $\gamma = 0.5$, $\mu_w = 0.8550$ *cp*, and $\mu_o = 0.0185$ *cp*. The density of the wetting phase (water) is $\rho_w = 1$ g/cm^3 and the density of the nonwetting phase (air) is considered negligible compared to ρ_w. These values were taken from [7].

The procedure consists in injecting a measured amount of radioactive water into the tube containing air in its pores, closing it off at both ends, and allowing the two phases to reach the equilibrium distribution. This saturation distribution is measured, providing the initial distribution in the simulation. This distribution is a spatial transition between air in the presence of residual water to water in the presence of residual air. This water saturation distribution results from the balance between pressure gradient and the buoyancy force.

Usage of the correct initial distribution of π is crucial to reproducing the results presented in [7]. To obtain this initial distribution from the procedure described in [7], we consider the injection of a certain quantity of water from the top of an air-saturated tube. Consequently, the lower half of the tube corresponds to an imbibition process and the upper half corresponds to a drainage process. The values of π are chosen accordingly. This choice of initial values for π are shown by the dotted line in Figure 5.5(a).

The tube is then inverted and measurements of water saturation are made during the segregation process at ten different locations along the tube. Figures 5.5(a)–(d) confirm the excellent agreement between the laboratory data and the simulated saturation profiles at different times, while Figures 5.6(a) and (b) show the importance of including the hysteresis effects in the model. There is agreement in Figure 5.6(a) with hysteresis and disagreement in Figure 5.6(b) without hysteresis.

6. Concluding remarks. We present Riemann solutions for each left and right state for a hysteretic counterflow segregation problem as well as criteria to guarantee well-posedness to the solution. Based on the Riemann solutions, we propose a corrected Godunov scheme that updates both the saturation and the hysteretic parameter. This scheme conserves mass locally. Numerically, we show that the solution

obtained by the proposed method agrees with the analytical solution. We also validate the numerical scheme by comparing simulations with laboratory experimental data. We show numerically that the inclusion of hysteresis effects in the relative permeability suffices for simulations for accurate simulations.

REFERENCES

[1] J. E. F. Altoé, *Modelagem Analítica do Processo de Migração Secundária de Hidrocarbonetos*, Master of Sciences Thesis, Universidade Estadual do Norte Fluminense, LENEP, Macaé, Rio de Janeiro, Brazil, 2002.

[2] K. Aziz and A. Settari, *Petroleum Reservoir Simulation*, Applied Science, London, 1979.

[3] J. Bear, *Dynamics of Fluids in Porous Media*, Elsevier, New York, 1972.

[4] P. Bedrikovetsky, *Mathematical Theory of Oil and Gas Recovery*, Kluwer Academic, London, 1993

[5] P. Bedrikovetsky, D. Marchesin, and P. R. Ballin, *Mathematical theory for two-phase displacement with hysteresis (with application to WAG injection)*, in Proceedings of the 5th European Conference on the Mathematics of Oil Recovery, Leoben, Austria, 1996.

[6] E. M. Braun and R. F. Holland, *Relative permeability hysteresis: Laboratory measurements and a conceptual model*, SPE Reservoir Engineering, 10 (1995), pp. 222–228 (paper 28615).

[7] J. E. Briggs and D. L. Katz, *Drainage of Water from Sand in Developing Aquifer Storage*, in Proceedings of the Fall Meeting of the Society of Petroleum Engineers of AIME, Dallas, TX, Society of Petroleum Engineers of AIME, 1966 (paper 1501-MS).

[8] J. Colonna, F. Brissaud, and J. L. Millet, *Evolution of capillarity and relative permeability hysteresis*, 253 (1972), pp. 28–38 (paper 2941-PA).

[9] R. E. Ewing, *The Mathematics of Reservoir Simulation*, Frontiers Appl. Math. 1, SIAM, Philadelphia, 1984.

[10] K. M. Furati, *Effects of relative permeability history dependence on two-phase flow in porous media*, Transp. Porous Media, 28 (1997), pp. 181–203.

[11] S. K. Godunov, *A finite difference method for the numerical computation of discontinuous solutions of the equations of fluid dynamics*, Mat. Sb., 47 (1959), pp. 271–290.

[12] J. E. Killough, *Reservoir simulation with history-dependent saturation functions*, SPE J., 1976, pp. 37–48 (paper 5106-PA).

[13] A. Kjosavik, J. K. Ringen, and S. M. Skjaeveland, *Relative permeability correlation for mixed-wet reservoirs*, SPE J., 7 (2002), pp. 49–58 (paper 77328-PA).

[14] R. J. LeVeque, *Numerical Methods for Conservation Laws*, Birkhäuser, Berlin, 1992.

[15] H. B. Medeiros, D. Marchesin, and P. L. Paes Leme, *Hysteresis in two-phase flow: A simple mathematical model*, Comput. Appl. Math., 17 (1998), pp. 81–99.

[16] O. A. Oleinik, *Uniqueness and stability of the generalized solution of the Cauchy problem for a quasilinear equation*, Uspekhi Mat. Nauk. 14 (1959), pp. 165–170. English translation in Amer. Math. Soc. Transl. Ser. 2, 33, AMS, Providence, RI, 1964, pp. 285–290.

[17] W. W. Owens and D. L. Archer, *The effect of rock wettability on oil-water relative permeability relationships*, J. Petroleum Tech. AIME, 1971, pp. 873–878 (paper 3034-PA).

[18] B. Plorh, D. Marchesin, P. Bedrikovetsky, and P. Krause, *Modeling hysteresis in porous media flow via relaxation*, Comput. Geosci., 5 (2001), pp. 225–256.

[19] N. Shahidzadeh-Bonn, E. Bertrand, J. P. Dauplait, J. C. Vié Borgotti, and D. Bonn, *Gravity drainage in porous media: The effect of wetting*, J. Petroleum Science & Engineering, 1085 (2003), pp. 1–8.

[20] E. E. Templeton, R. F. Nielsen, and C. D. Stahl, *A study of gravity counterflow segregation*, SPE J., 1962, pp. 186–193 (paper 186-PA).